PAPER

Sound Field Reproduction by Wavefront Synthesis Using Directly Aligned Multi Point Control

Noriyoshi KAMADO[†a)], *Nonmember*, **Haruhide HOKARI**[††b)], **Shoji SHIMADA**[††c)], **Hiroshi SARUWATARI**[†], *and* **Kiyohiro SHIKANO**[†], *Members*

SUMMARY In this paper, we present a comparative study on directly aligned multi point controlled wavefront synthesis (DMCWS) and wave field synthesis (WFS) for the realization of a high-accuracy sound reproduction system, and the amplitude, phase and attenuation characteristics of the wavefronts generated by DMCWS and WFS are assessed. First, in the case of DMCWS, we derived an optimal control-line coordinate based on a numerical analysis. Next, the results of computer simulations revealed that the wavefront in DMCWS has wide applicability in both the spatial and frequency domains with small amplitude and phase errors, particularly above the spatial aliasing frequency in WFS, and we clarified that the amplitude error in DMCWS has similar behavior to the well-known approximate expression for spatial decay in WFS; this implies the ease of taking into account estimating the amplitude error in DMCWS. Finally, we developed wavefront measurement system and measured a DMCWS wavefront using our wavefront measurement system and algorithm. The results of measurements clarified the frequency characteristics of a loudspeaker. Also, DMCWS has wide applicability in frequency domains in actual environments. From these findings, we concluded the advantageousness of DMCWS compared with WFS.

key words: *wavefront synthesis, wavefront measurement, impulse response, multi-point control*

1. Introduction

In recent years, there has been increasing research interest in wavefront synthesis, which enables multiple sound sources to create a sound field that is identical to any original sound field. It is expected to provide a wider effective listening area than the current 5.1 system or a surround system with many channels, which means that the listener can perceive the same sound image regardless of the listening position.

Wavefront synthesis techniques can be classified into various types; typical methods are wave field synthesis (WFS) [1] and directly-aligned multi-point controlled wavefront synthesis (DMCWS) [2], [3]. Although the theory of WFS has been well studied, the optimal control-point geometry and the behavior of the synthesized secondary wavefront within and above the frequency bandlimit in DMCWS have not been investigated so far. Therefore, in this paper, we describe the implementation of DMCWS and evaluate its effectiveness through the comparison with WFS. Since the wavefront has the frequency characteristics of actual audio applications, we determine the spatial spectrum characteristics of DMCWS in an actual environment. Hence, we derive the spatial spectrum characteristics from the impulse responses at each observation point and measure the DMCWS wavefront using a wavefront measurement system [4] in an actual environment.

The rest of this paper is organized as follows. In Sect. 2, the principles of WFS and DMCWS are explained. In Sect. 3, the optimum directly-aligned control point coordinates are described. In Sect. 4, the quantitative comparison of DMCWS with WFS is described in relation to their numerically calculated wavefronts. In Sect. 5, wavefront synthesis and measurement experiments in an actual environment are described. Following a discussion on the results of the experiments, we present our conclusions in Sect. 6.

Manuscript received June 17, 2010.
Manuscript revised November 15, 2010.

[†]The authors are with Nara Institute of Science and Technology, Ikoma-shi, 630-0192 Japan.
[††]The authors are with Nagaoka University of Technology, Nagaoka-shi, 940-2188 Japan.
a) E-mail: noriyoshi-k@is.naist.jp
b) E-mail: hokari@vos.nagaokaut.ac.jp
c) E-mail: shimada@vos.nagaokaut.ac.jp

DOI: 10.1587/transfun.E94.A.907

2. Theory

2.1 WFS

In this section, WFS and MCWS (DMCWS) are described theoretically and the equations used for numerical calculations are derived in detail. The geometric configuration and parameters in WFS are depicted in Fig. 1, where $S_P(\omega)$ and $S_{Sn}(\omega)$ denote the spectra of the primary and the nth secondary sources, respectively, on the x-y horizontal plane.

The spectrum of the nth secondary source, which synthesizes the primary spherical wavefront, is expressed as [5], [6]

$$S_{Sn}(\omega) =$$

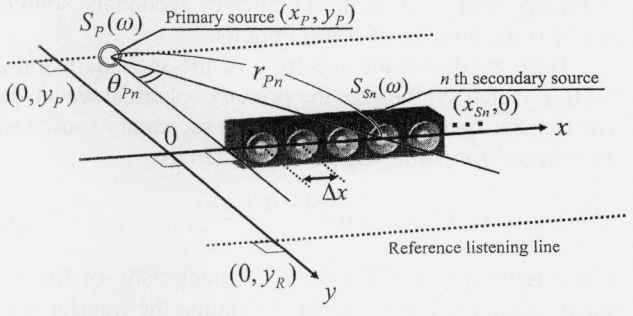

Fig. 1 Configuration of WFS.

$$\sqrt{\frac{\mathrm{j}k}{2\pi}}C(y_R, y_P)\frac{\exp(-\mathrm{j}kr_{Pn})}{\sqrt{r_{Pn}}}\Delta x S_P(\omega)\frac{\cos\theta_{Pn}}{G(\theta_{Pn},\omega)}, \quad (1)$$

where j is the imaginary unit, k is the wavenumber (ω/c), c is the sound velocity, ω denotes the angular frequency, Δx is the interelement interval among the secondary sources, r_{Pn} is the distance between the primary source and the nth secondary source, and θ_{Pn} is the angle between the y-axis and the line connecting the nth secondary and primary sources. $G(\theta_{Pn}, \omega)$ is a distance-independent directivity function defined only under far-field conditions. $C(y_R, y_P)$ is a function that compensates the level of mismatch due to the stationary phase approximation along the x-direction [7], which is a function of only the reference listening distance y_R [8] and is given as

$$C(y_R, y_P) = \sqrt{\frac{|y_R|}{|y_R - y_P|}}. \quad (2)$$

Outside the reference listening line, the level of the sound field is expressed as

$$Att_S(y) = \sqrt{\frac{|y_R|}{|y|}}\sqrt{\frac{|y| + |y_P|}{|y_R| + |y_P|}}\frac{1}{|y - y_P|}. \quad (3)$$

2.2 DMCWS

The geometric parameters of MCWS are shown in Fig. 2. MCWS controls the spatial spectra at the control points, which are randomly located on the x-y horizontal plane in front of the secondary sources, and generates the desired wavefront. In MCWS, there is one typical case in which each control point is located on the control line parallel to the x-axis and intersecting the y-axis at y_C (its geometric parameters are depicted in Fig. 3 [3]). In this case, the wavefront synthesis method is called DMCWS (Directly-aligned MCWS), named after its control-point geometry. Here, $S_{Cm}(\omega)$ denotes the secondary wavefront spectrum at the mth control-point position. Also, θ_{Cm} is the angle between the y-axis and the line connecting the mth control point and the primary source, θ_{Snm} is the angle between the y-axis and the line connecting the mth control point and the nth secondary source, r_{Cm} is the spatial distance between the mth control point and the primary source, r_{Snm} is the spatial distance between the mth control point and the nth secondary source, N is the number of secondary sources, and M is the number of control points.

Here we derive the spectrum of the secondary source $S_{Sn}(\omega)$, which synthesizes the primary spherical wavefront. The transfer function between the nth secondary source and the mth control point, $H_{nm}(\omega)$, is written as

$$H_{nm}(\omega) = G(\theta_{Snm}, \omega)\frac{\exp(-\mathrm{j}kr_{Snm})}{r_{Snm}}, \quad (4)$$

where $G(\theta, \omega)$ is the directivity characteristic of the secondary sources. From Eq. (4), we define the transfer function matrix

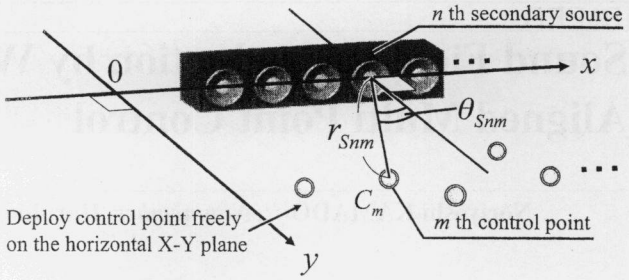

Fig. 2 Configuration of MCWS.

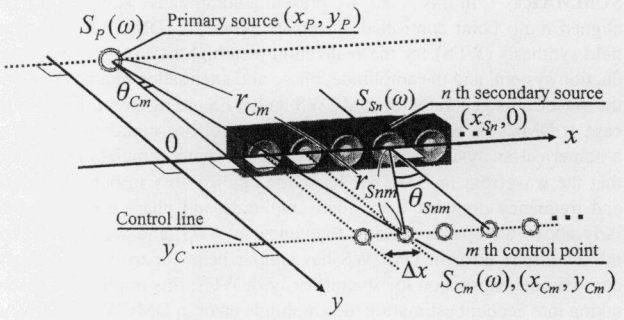

Fig. 3 Configuration of DMCWS.

$$\boldsymbol{H}(\omega) = \begin{bmatrix} H_{1,1}(\omega) & \cdots & H_{N,1}(\omega) \\ H_{1,2}(\omega) & \cdots & H_{N,2}(\omega) \\ \vdots & \ddots & \vdots \\ H_{1,M}(\omega) & \cdots & H_{N,M}(\omega) \end{bmatrix}. \quad (5)$$

We write the secondary wavefront spectrum vector at the mth control-point position as

$$\boldsymbol{S_C}(\omega) = \boldsymbol{H}(\omega)\boldsymbol{S_S}(\omega), \quad (6)$$

where

$$\boldsymbol{S_C}(\omega) = [S_{C1}(\omega), S_{C2}(\omega), \cdots, S_{CM}]^{\mathrm{T}}, \quad (7)$$

$$\boldsymbol{S_S}(\omega) = [S_{S1}(\omega), S_{S2}(\omega), \cdots, S_{SN}]^{\mathrm{T}}, \quad (8)$$

and $\cdot^{\mathrm{T}}$ denotes the transpose of the vector/matrix. If the primary wavefront spectrum is equal to the secondary wavefront spectrum at the control-point position, Eq. (6) can be transformed into

$$\boldsymbol{S_C}(\omega) = \boldsymbol{P}(\omega)S_P(\omega), \quad (9)$$

where

$$\boldsymbol{P}(\omega) = \left[\frac{e^{-\mathrm{j}kr_{C_1}}}{r_{C_1}}, \frac{e^{-\mathrm{j}kr_{C_2}}}{r_{C_2}}, \cdots, \frac{e^{-\mathrm{j}kr_{C_M}}}{r_{C_M}}\right]^{\mathrm{T}}. \quad (10)$$

From Eqs. (6) and (9) and the generalized inverse matrix of $\boldsymbol{H}(\omega)$, $\boldsymbol{H}^{+}(\omega)$, we obtain the secondary source spectrum vector in the following form;

$$\boldsymbol{S_S}(\omega) = \boldsymbol{H}^{+}(\omega)\boldsymbol{P}(\omega)S_P(\omega). \quad (11)$$

3. Optimized Control Point Geometry

The secondary wavefront spectrum vector in DMCWS contains the control line geometry, and its optimal geometry has not been elucidated completely. Hence we study its geometry through a wavefront calculation in this section.

3.1 Calculation Conditions

The conditions of the wavefront calculation are shown in Table 1. The diaphragm radius b and secondary source distance Δx mimic those of the Soundevice SD-0.6 loudspeaker shown in Fig. 4. The spatial aliasing frequency in front of the center of the array of the loudspeakers is given as

$$f_{alias} = \frac{c}{2\Delta x} = \frac{340.64}{2 \times 0.12} \simeq 1417 \quad [\text{Hz}], \tag{12}$$

where Δx denotes the distance from the loudspeaker and c denotes the sound velocity. The inter-aural time differences (ITD) which are obtained by evaluated wavefront band frequencies below 1600 Hz are major cues for sound source localization [9]. The geometric parameters in the wavefront calculation are illustrated in Fig. 5. In addition, the number of secondary sources is determined by the hardware limitation. In terms of the control area, the more control points, the better. However, under the terms of $N < M$, the rank-deficient problem occur in the transfer function matrix $\boldsymbol{H}(\omega)$ and the reproduction accuracy becomes diminished. Therefore, we set the number of control points to the maximum value which satisfies $N \geq M = 16$.

Table 1 Wavefront calculation conditions.

PARAMETER	VALUE
Temperature	15℃
Sound velocity c	340.64 m/s
Evaluated wavefront band frequencies	20–1600 Hz (10 Hz interval)
Spatial aliasing frequency	1417 Hz
Primary source geometry (x_P, y_P)	(1.2, −0.1—1.0) m
Secondary source and Control point interval Δx	0.12 m
Diaphragm radius b	0.05 m
Number of secondary sources N and Control points M	16
y-coordinate of control line y_C	0.1–2.0 m

Fig. 4 Soundevice SD-0.6 loudspeaker, whose diaphragm radius and source distance were assumed in the experiment.

3.2 Method of Calculating Secondary Wavefront

The secondary source and observation point geometric parameters are shown in Fig. 6. Equation (13) defines $S_O(\omega)$, which denotes the spectrum of the secondary wavefront at the observation point, given as

$$S_O(\omega) = \sum_{n=1}^{N} \left[S_{Sn}(\omega) G(\theta_{On}, \omega) \frac{\exp(-\mathrm{j}kr_{On})}{r_{On}} \right]. \tag{13}$$

The secondary sources are circular vibration planes on an infinite baffle whose directional characteristic is

$$G(\theta, \omega) = \frac{2J_1(kb \sin\theta)}{kb \sin\theta}, \tag{14}$$

where $J_1(\cdot)$ is the Bessel function of the first kind and b is the diaphragm radius of each circular vibration plane.

3.3 Evaluation Criterion of Secondary Wavefront

$E_{wf}(y_P, y_C)$ is the criterion used for evaluating the reproduced wavefront accuracy,

$$E_{wf}(y_P, y_C) = 10 \log_{10} \frac{\sum_{i,j} \sum_{\omega} \{|\mathrm{SWF}(i, j, \omega)| - |\mathrm{PWF}(i, j, \omega)|\}^2}{\sum_{i,j} \sum_{\omega} |\mathrm{PWF}(i, j, \omega)|^2} \quad [\text{dB}], \tag{15}$$

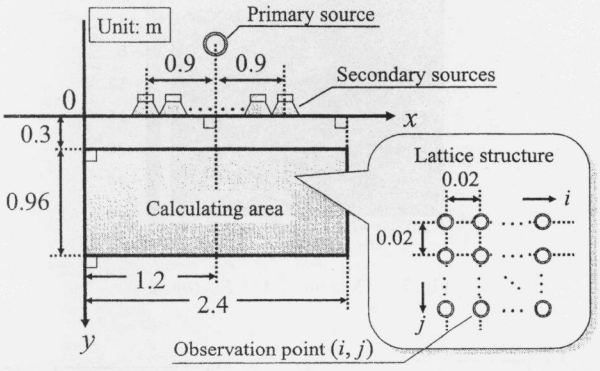

Fig. 5 Geometric parameters in wavefront calculation.

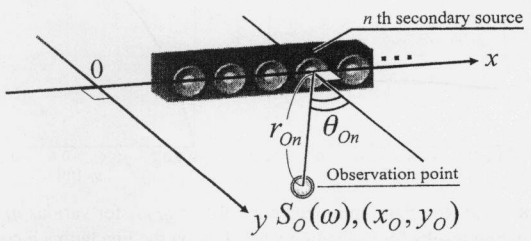

Fig. 6 Secondary source and observation point geometric parameters.

where $\mathrm{PWF}(i, j, \omega)$ is a function of the primary wavefront spectrum at the observation point (i, j);

$$\mathrm{PWF}(i, j, \omega) = \frac{\exp\left(-\mathrm{j}kr_{O(i,j)}\right)}{r_{O(i,j)}}, \tag{16}$$

where $r_{O(i,j)}$ is the spatial distance between the primary source and the observation point (i, j). $\mathrm{SWF}(i, j, \omega)$ is a function of the DMCWS secondary wavefront spectrum at the same position. Here, $\sum_{\omega}$ is the summation over ω in the evaluation frequency band, and $\sum_{i,j}$ is the summation over the observation position (i, j). In this paper, we define the optimal control line geometry y_{Copt} as

$$y_{Copt}(y_P) = \underset{y_C}{\mathrm{argmin}}\, E_{wf}(y_P, y_C), \tag{17}$$

where $\mathrm{argmin}_{y_C} \cdot$ denotes the minimization function. We calculate the optimal control line geometry y_{Copt} with numerical simulation.

3.4 Calculation Results

Figure 7 shows the results of the calculation, where the contour lines show values of $E_{wf}(y_P, y_C)$ with an interval of 2 dB. Figure 8 shows y_P for the optimized y_C, and the corresponding value of $E_{wf}(y_P, y_C)$. Figure 8(a) shows that when y_C is optimized, the y-coordinate y_{Copt} ranges from 0.6 to 0.7 m for the synthesized secondary wavefront. Also, Fig. 8(b) shows an increase in the evaluation criterion E_{wf} with the primary source y-coordinate y_P, and that the value

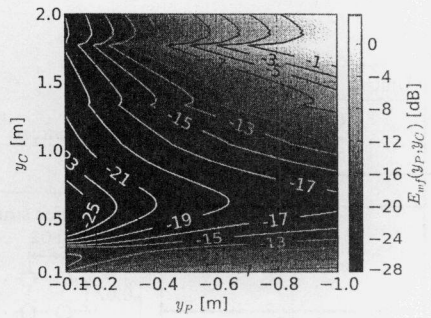

Fig. 7 Contour plot of $E_{wf}(y_P, y_C)$.

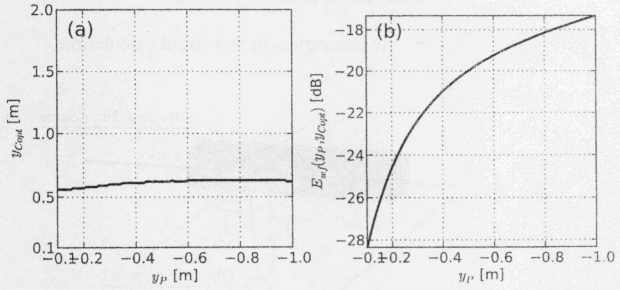

Fig. 8 (a) Resultant optimized control line y_{Copt} for various y_P and (b) calculation results for evaluation value E_{wf} on the line with a y-coordinate of y_{Copt}.

of y_P which minimize E_{wf} in Fig. 8(b) is 0.1 m. Hence, we define the control line coordinate y_{Copt} as 0.6 m when the primary y-coordinate y_P is 0.1 m according to the condition shown in Fig. 5. We decided to use these values in the subsequent computer simulations.

4. Computer-Simulation Based Comparison of DMCWS and WFS

4.1 Calculation Conditions

In this section, we compare DMCWS and WFS through computer-simulation-based experiments in terms of the amplitude, phase, and attenuation of the synthesized secondary wavefront spectrum. The wavefront calculation conditions are listed in Table 2 and the other conditions are the same as those in Table 1 and Fig. 5.

4.2 Evaluation Criteria of Secondary Wavefront

The evaluation criteria $E_A(i, j)$ and $E_P(i, j)$ used to evaluate the complex amplitude and phase errors of the secondary wavefront are respectively defined as

$$E_A(i, j) = 10 \log_{10} \frac{\sum_{\omega} \{|\mathrm{WF}(i, j, \omega)| - |\mathrm{PWF}(i, j, \omega)|\}^2}{\sum_{\omega} |\mathrm{PWF}(i, j, \omega)|^2} \ [\mathrm{dB}], \tag{18}$$

$$E_P(i, j) = 10 \log_{10} \frac{1}{K} \sum_{\omega} \left| \frac{1}{\pi} \arg\left(\frac{\mathrm{PO}(\mathrm{WF}(i, j, \omega))}{\mathrm{PO}(\mathrm{PWF}(i, j, \omega))} \right) \right| \ [\mathrm{dB}], \tag{19}$$

where $\mathrm{WF}(i, j, \omega)$ denotes the secondary wavefront synthesized by DMCWS or WFS, K is the number of frequency bins and $\mathrm{PO}(\cdot)$ denotes the phase function given by

$$\mathrm{PO}(x) = \frac{x}{|x|}, \tag{20}$$

where x is a complex-valued variable.

4.3 Calculation Results

Figures 9 and 10 show the amplitude error E_A of WFS and

Table 2 Calculation conditions used in evaluation of DMCWS and WFS.

PARAMETER	VALUE
Primary source geometry (x_P, y_P)	(1.2, −0.1), (1.2, −0.7) m
Control line y-coordinate y_C	0.6 m
Evaluated wavefront band frequencies	20–1400 and 20–1600 Hz (10 Hz interval)
Reference listening distance y-coordinate y_R	0.6 m

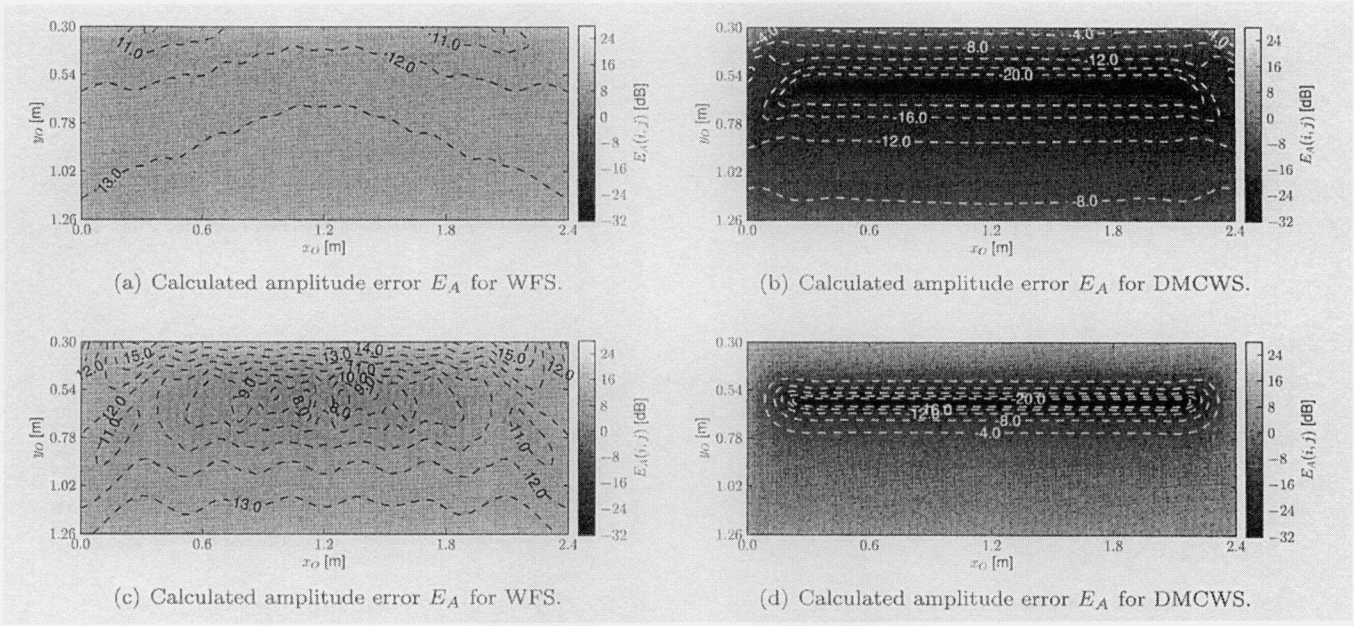

Fig. 9 Comparison of the calculated E_A of WFS and DMCWS. The evaluated frequency bands are 20–1400 Hz. The primary source geometry of (a) and (b) are $(x_P, y_P) = (1.2, -0.1)$, and (c) and (d) are $(x_P, y_P) = (1.2, -0.7)$.

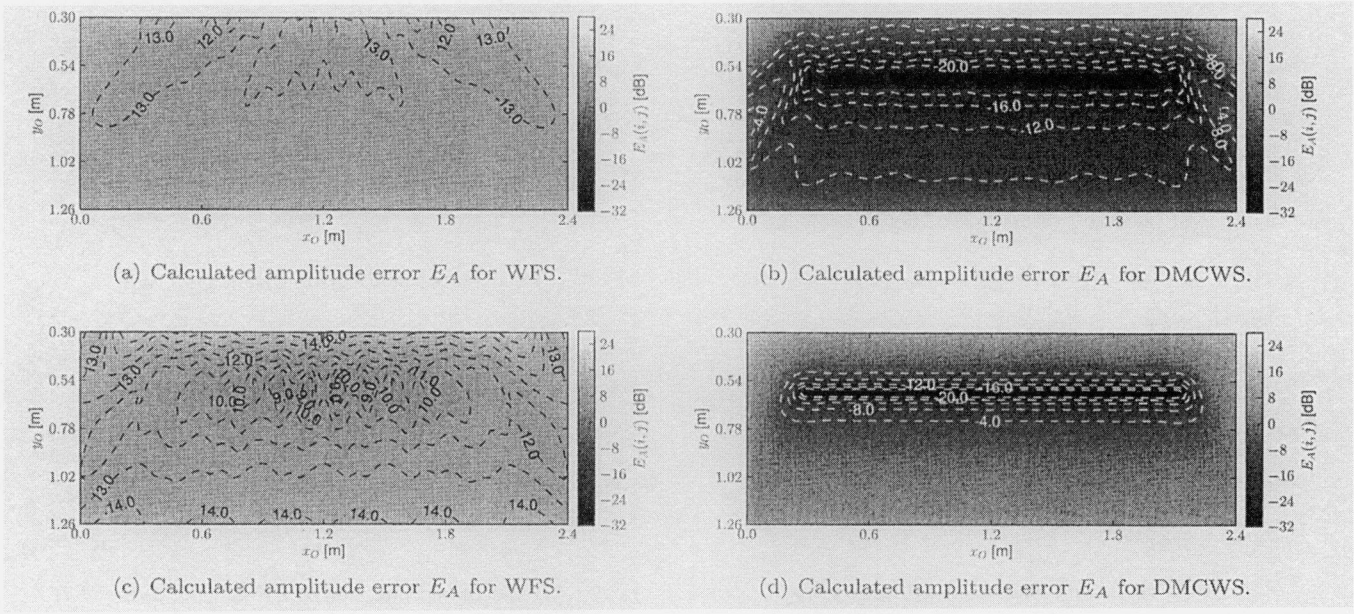

Fig. 10 Comparison of the calculated E_A of WFS and DMCWS. The evaluated frequency bands are 20–1600 Hz. The primary source geometry of (a) and (b) are $(x_P, y_P) = (1.2, -0.1)$, and (c) and (d) are $(x_P, y_P) = (1.2, -0.7)$.

DMCWS that of the evaluated wavefront band frequencies is 20–1400 Hz and 20–1600 Hz, respectively. The values of E_A are given on the contour lines, and the intervals between the contour lines are 1.0 dB in Figs. 9(a) and 9(c) and 4.0 dB in Figs. 10(b) and 10(d). As can be seen in Figs. 9 and 10, the amplitude error of WFS is serious by comparison with that of DMCWS both for the upper-limit of the evaluation frequency band which are below and above the spatial aliasing frequency (1417 Hz). In contrast, in Figs. 9(b), 9(d), 10(b) and 10(d), the amplitude error of DMCWS is from −8 to −20 dB, which is small in comparison with that of WFS, and is generally smallest in the vicinity of the control points. The amplitude error difference between the results of WFS and that of DMCWS indicates 60–120 dB around the control points.

Figures 11 and 12 show the phase error E_P of WFS and DMCWS that of the evaluated wavefront band frequencies is 20–1400 Hz and 20–1600 Hz, respectively. The values of E_P are given on the contour lines, and the intervals between the contour lines are 1.0 dB in Figs. 11(a), 11(c), 12(a) and

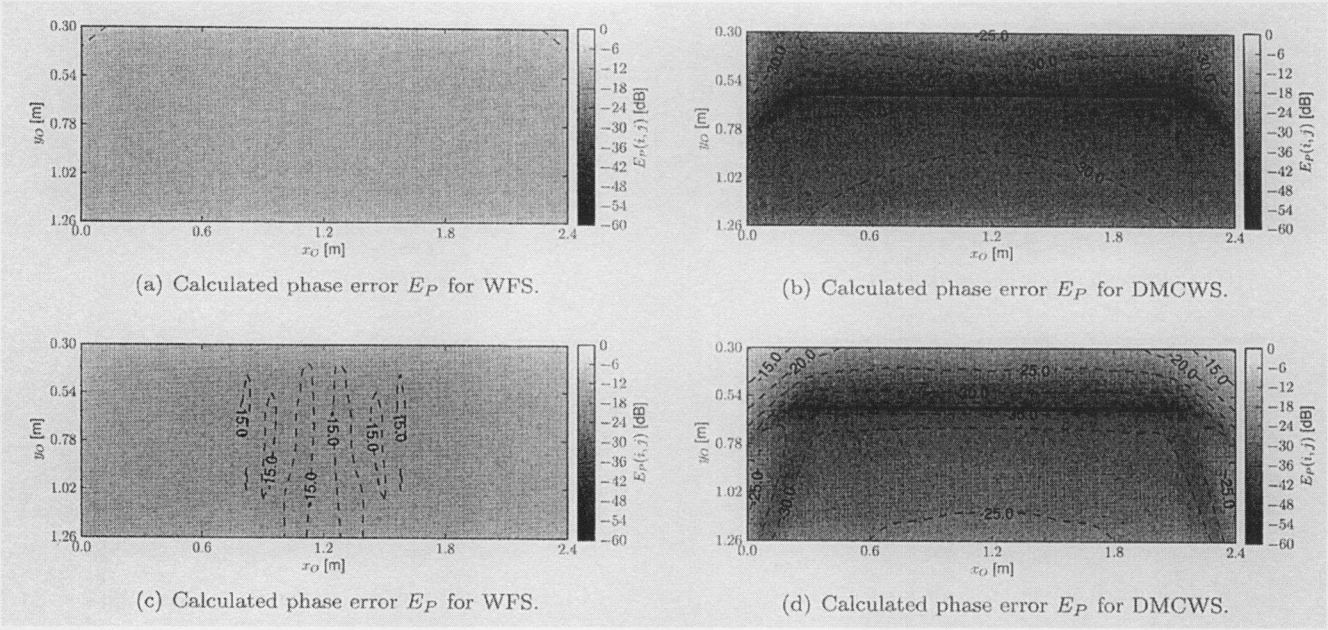

Fig. 11 Comparison of the calculated E_P of WFS and DMCWS. The evaluated frequency bands are 20–1400 Hz. The primary source geometry of (a) and (b) are $(x_P, y_P) = (1.2, -0.1)$, and (c) and (d) are $(x_P, y_P) = (1.2, -0.7)$.

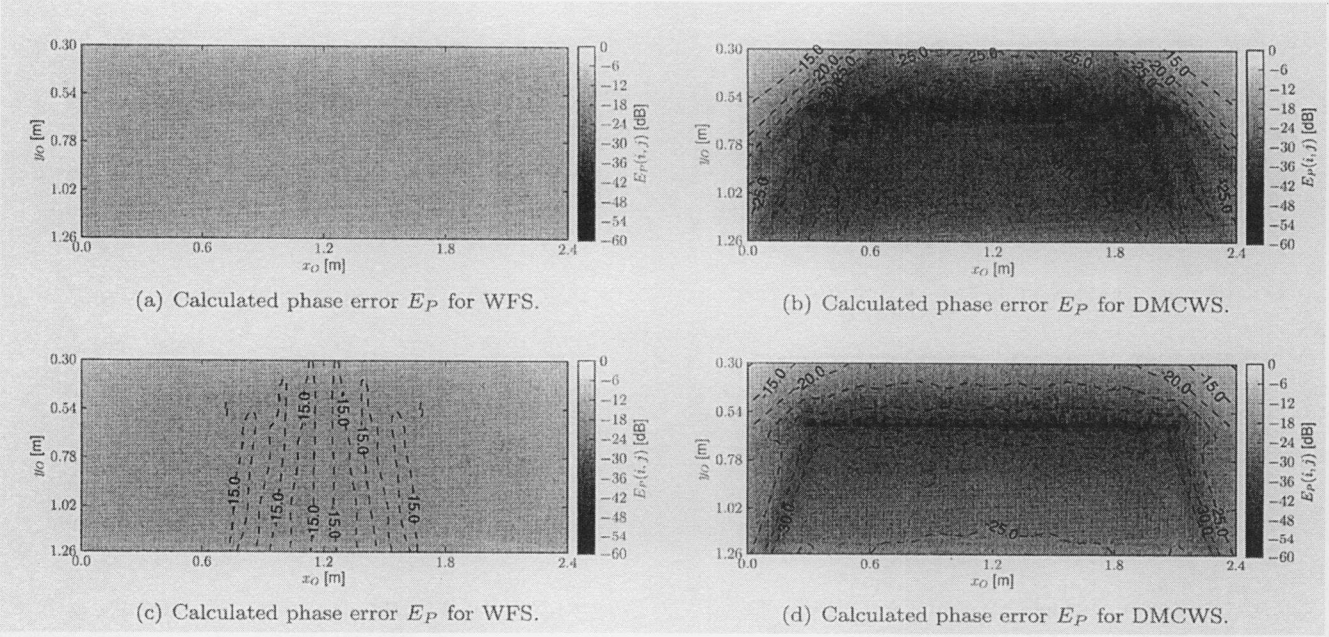

Fig. 12 Comparison of the calculated E_P of WFS and DMCWS. The evaluated frequency bands are 20–1600 Hz. The primary source geometry of (a) and (b) are $(x_P, y_P) = (1.2, -0.1)$, and (c) and (d) are $(x_P, y_P) = (1.2, -0.7)$.

12(c) and 2.0 dB in Figs. 11(b), 11(d), 12(b) and 12(d). According to Figs. 11 and 12, there is a significant phase error E_P by comparison with that of DMCWS, similar to the amplitude error shown in Figs. 9 and 10, in the case of WFS. In contrast, there is an extremely small phase error in DMCWS, as shown in Figs. 11(b), 11(d), 12(b) and 12(d).

In Figs. 9 and 10, the amplitude error and the phase error is smaller than that of WFS.

We next calculate the attenuation to examine the characteristic of the wavefront amplitude error. Figure 13 shows the attenuations of the primary wavefront and the WFS and DMCWS secondary wavefronts, as well as Att_{S_S} (see Eq. (3)) in front of the primary source at the upper-limit frequency of the evaluation band (1600 Hz). To determine the effect of the y-coordinate of the primary source y_P on wavefront attenuation, we calculate the attenuation for y_P of -0.1 and -0.7 m, as shown in Figs. 13(a), (c) and 13(b), (d), respectively. The attenuation plot for WFS undergoes greater fluctuation than the other attenuation plots in Figs. 13(c) and (d), because the evaluation frequency of 1600 Hz is above

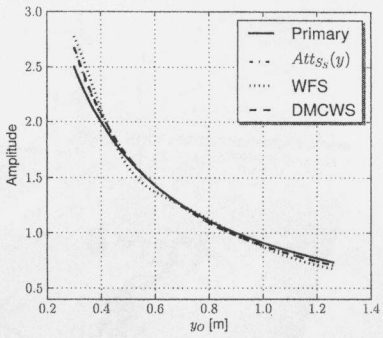

(a) Primary source is located at $(x_P, y_P) = (1.2, -0.1)$ m and wavefront frequency is 1400 Hz.

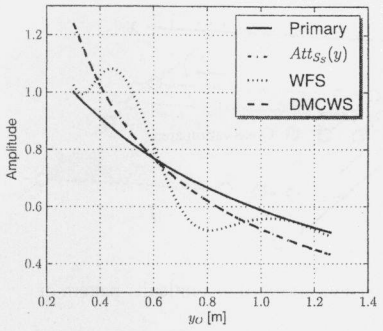

(b) Primary source is located at $(x_P, y_P) = (1.2, -0.7)$ m and wavefront frequency is 1400 Hz.

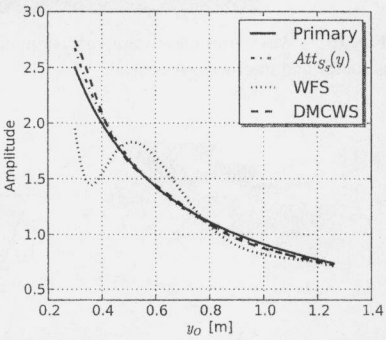

(c) Primary source is located at $(x_P, y_P) = (1.2, -0.1)$ m and wavefront frequency is 1600 Hz.

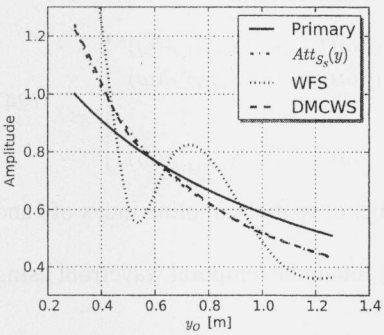

(d) Primary source is located at $(x_P, y_P) = (1.2, -0.7)$ m and wavefront frequency is 1600 Hz.

Fig. 13 Comparison of attenuation in front of primary source.

the spatial aliasing frequency (1417 Hz). On the other hand, the amplitude in DMCWS undergoes little fluctuation compared with that in WFS, suggesting the applicability of DMCWS in frequency bands higher than the spatial aliasing frequency. Also, Fig. 13 shows that the attenuation in DMCWS is very similar to Att_{S_S} rather than that of the primary sound source. This result implies the possibility that spatial decay [6] occurs in DMCWS in the same way as it does in WFS, suggesting the ease of estimating the amplitude error in DMCWS.

5. Evaluation in Actual Environment

The numerical evaluation results in the previous section clarify the effectivity of the wavefront synthesized with DMCWS. In this section, we measure the wavefront to verify the numerical evaluation results of DMCWS in actual environment.

5.1 Spatial Spectrum Characteristics Obtained from Impulse Responses

In this section, we propose a wavefront measurement method using the spatial spectrum characteristics obtained from the impulse response at each observation point.

The wavefront spectrum characteristics (Eq. (13)) at the observation point $S_O(\omega)$ are expressed below in vector form:

$$\begin{aligned} S_O(\omega) &= \boldsymbol{Q}^{\mathrm{T}}(\omega)\boldsymbol{S}_S(\omega) \\ &= \boldsymbol{Q}^{\mathrm{T}}(\omega)\boldsymbol{H}^{+}(\omega)\boldsymbol{P}(\omega)S_P(\omega) \\ &= S_{arr}(\omega)S_P(\omega), \end{aligned} \tag{21}$$

where

$$\boldsymbol{Q}(\omega) = [Q_1(\omega), Q_2(\omega), ..., Q_N(\omega)]^{\mathrm{T}}, \tag{22}$$

$$Q_n(\omega) = G_{Sn}(\theta_{On}, \omega)\frac{\exp(-\mathrm{j}kr_{On})}{r_{On}}. \tag{23}$$

$Q_n(\omega)$ is the radiation characteristic of the nth sound source at the azimuth angle θ for angular frequency ω, and the loudspeaker array characteristic $S_{arr}(\omega)$ is assumed to be the radiation characteristic of a single sound source.

Hence, we can estimate the spectrum characteristic of a loudspeaker array $S_{arr}(\omega)$ using an acoustic impulse response measurement method with a signal input to a primary source $S_P(\omega)$ and a signal output signal at the observation point $S_O(\omega)$. The set of spatial spectrum characteristic of loudspeaker array $S_{arr}(\omega)$ in the observation area around construct wavefront, since we can estimate the spatial spectrum characteristic of synthesized secondary wavefront to measure the set of $S_{arr}(\omega)$.

Figure 14 shows observation area arranged in a reticu-

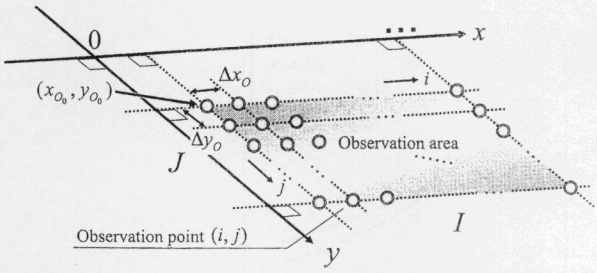

Fig. 14 The observation area arranged in a reticular pattern of observation point.

lar pattern of observation point. In Fig. 14, the set of spectrum characteristic of synthesized secondary wavefront at each observation point in matrix form:

$$\boldsymbol{S}_{arr}(\omega) = \begin{bmatrix} S_{arr(1,1)}(\omega) & \cdots & S_{arr(1,J)}(\omega) \\ S_{arr(2,1)}(\omega) & \cdots & S_{arr(2,J)}(\omega) \\ \vdots & \ddots & \vdots \\ S_{arr(I,1)}(\omega) & \cdots & S_{arr(I,J)}(\omega) \end{bmatrix}. \quad (24)$$

I and J is the total number of spatial sampling index of i and j, respectively.

From Eq. (24), we obtain the temporal wavefront using inverse fourier transform;

$$\begin{aligned} \boldsymbol{s}_{\mathrm{arr}}(t) &= \frac{1}{2\pi}\int_{-\infty}^{\infty} \boldsymbol{S}_{arr}(\omega)e^{j\omega t}d\omega \\ &= \begin{bmatrix} s_{arr(1,1)}(t) & \cdots & s_{arr(1,J)}(t) \\ s_{arr(2,1)}(t) & \cdots & s_{arr(2,J)}(t) \\ \vdots & \ddots & \vdots \\ s_{arr(I,1)}(t) & \cdots & s_{arr(I,J)}(t) \end{bmatrix}. \end{aligned} \quad (25)$$

In this paper, we estimate $S_{arr}(\omega)$ using the M-sequence method [10] to measure the acoustic impulse response.

5.2 Wavefront Measurement System

Figure 15 shows the wavefront measurement system for visualization of the wavefront obtained by Eq. (24).

The measuring microphones are placed on the electric two axes actuator so that the microhpones can move around the horizontal plane in front of the loudspeaker array and measure the spectrum characteristics $S_{arr(i,j)}(\omega)$. In addition, we use a linear microphone array to save the amount of time spent for measurement. The interval of the microphones is 0.48 m and the total number of microphones is 4, i.e., microphone array width is 1.44 m, and the microphones are audio-technica ATM14a omnidirectional microphones. The electric actuator has 0.96 m range of movement on each axis. As a result, the width (x-axis) and height (y-axis) of the observation area are 2.4 m and 0.96 m, respectively.

Figure 16 shows the procedure used to construct resultant all wavefronts of all the observation areas from measured wavefront at each observation area. The wavefront constructed in all the observation areas, shown in Fig. 16(b), can be obtained as an overlap of each wavefront measured from adjacent microphones, shown in Fig. 16(a).

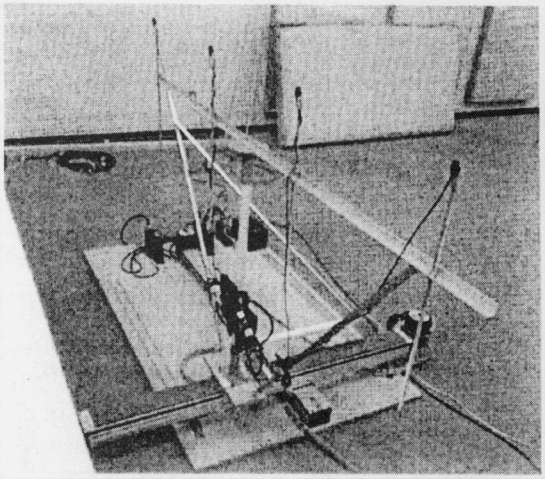

Fig. 15 Wavefront measurement system consists of electric two axes actuator and microphone array.

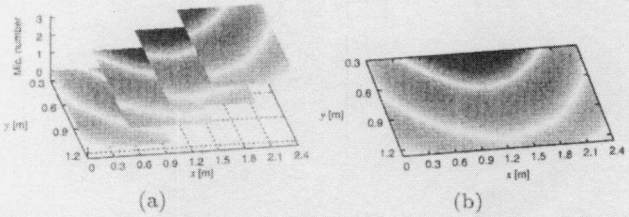

Fig. 16 The procedure used to construct all wavefront of all the observation areas from measured wavefront at each observation area. (a) Before coupling the wavefront measured by each microphone observation area. (b) The wavefront after coupling process.

5.3 Wavefront Measurement Conditions

Table 3 shows the wavefront measurement conditions. The control line y-coordinate y_C is set to 0.6 m.

The order L of M-Sequence is determined by the relation between measurement room's reverberation time T_r and sampling frequency f_s as

$$L \geq \lceil \log_2(f_s T_r) \rceil, \quad (26)$$

where $\lceil \cdot \rceil$ denotes ceiling function. Table 3 and Eq. (26) show $L \geq \lceil \log_2(48000 \times 0.3) \rceil = 14$, and consequently we use $L = 15$ in this paper.

5.4 Results of Wavefront Measurement

Figures 17 and 18 show the calculate and measured wavefronts obtained using DMCWS, respectively. Compared with Fig. 17, we can see a clearer interference pattern in Fig. 18. Figures 19 and 20 show the calculated and measured frequency-amplitude characteristics in front of the center of the loudspeaker array, respectively. In Fig. 20, a pattern due to the interference can also be observed.

Table 3 Wavefront measurement conditions.

PARAMETER	VALUE
Measurement room	Nagaoka University of Technology Acoustically isolated room W 5.3×H 9.5×D 4.3 m Reverberation time T_r 0.3 s
Room temperature	15℃
Sound velocity c	340.64 m/s
Primary source geometry (x_P, y_P)	(1.2,-0.1) m
Wavefront drawing sample	31 samples
Sampling frequency f_s	48 kHz
Wavefront synthesis method	DMCWS
Synchronous addition count	40 cycles
Secondary source	Soundevice SD–0.6
Secondary source order N	16
Source distance Δx	0.12 m
Spatial aliasing frequency f_{alias}	1417 Hz
Measured wavefront band frequencies	200–24000 Hz
Height of secondary sources	1.22 m

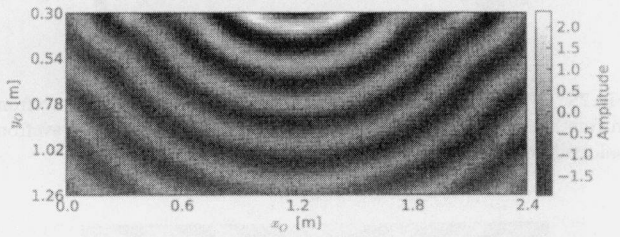

Fig. 17 Calculated secondary wavefront (1600 Hz).

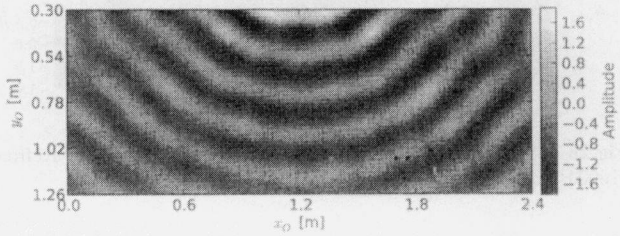

Fig. 18 Measured secondary wavefront (1600 Hz).

5.5 Effects of Room Reflection

In the soundproof room used in this measurement, we consider that the wave reflected by the wall affects the secondary synthesized wavefront. The reflection surface nearest to the source is the floor of this room. The relation between the direct and reflected waves generated by the primary source is obtained by the *image method* [11], where the line $y = 0$ corresponds to the floor. In the image method the reflected wave is generated by an imaginary source located at the reflection of the primary source in the line $y = 0$. In the image method, we can regard the reflected wave as a direct wave generated from this imaginary point source. Us-

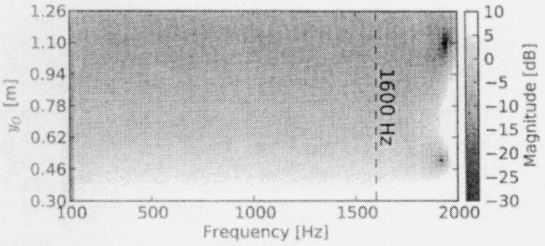

Fig. 19 Calculated frequency amplitude characteristics in front of center of loudspeaker array.

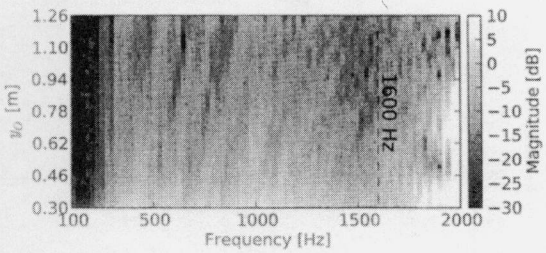

Fig. 20 Measured frequency amplitude characteristics in front of center of loudspeaker array.

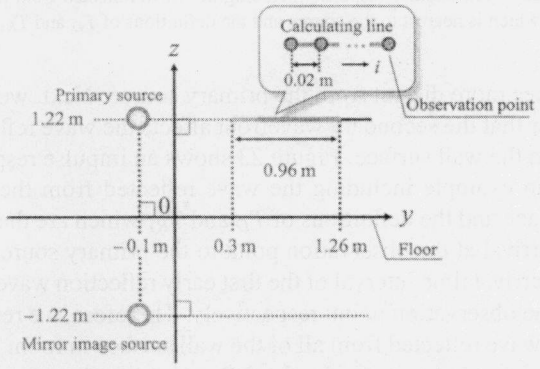

Fig. 21 Calculation conditions used to determine the effect of the wave reflected from the floor surface.

Table 4 Calculation conditions for primary source wavefront and the wavefront reflected from the floor surface.

PARAMETER	VALUE
Room temperature	15℃
Sound velocity c	340.64 m/s
Sampling frequency f_s	48 kHz
Primary sound source model	Point source

ing the image method, we can consider the effect of waves reflected from the floor, and we calculate the primary wavefront using this method. Figure 21 and Table 4 show the calculation conditions.

Figure 22 shows the frequency characteristics of the wavefront calculated with the primary source and the reflected wave obtained by the image method. This result shows that the wave reflected from the floor surface causes an interference pattern in the frequency characteristics, which tends to broaden as the observation point be-

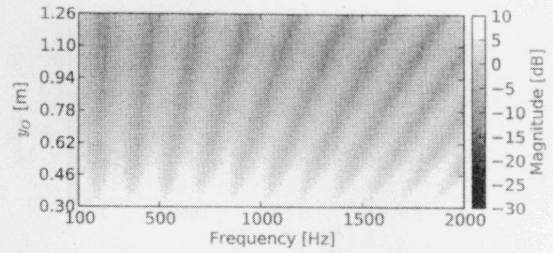

Fig. 22 Frequency characteristics of primary source wavefront and the wavefront reflected from the floor surface calculated with the image method.

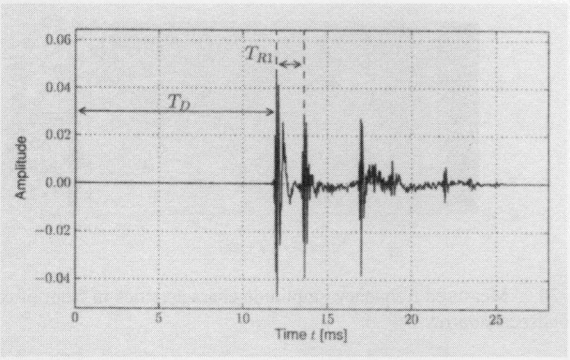

Fig. 23 An impulse response including the wave reflected from the surface which is nearest to the source and the definitions of T_D and T_{R1}.

comes more distant from the primary source. Next, we consider that the secondary wavefront affects the wave reflected from the wall surface. Figure 23 shows an impulse response as an example including the wave reflected from the wall surface and the definitions of T_D and T_{R1} which are the time of arrival at the observation point to the primary source and the arrival time interval of the first early reflection wavefront at the observation point, respectively. Therefore, we remove the wave reflected from all of the wall surface in room using hanning window given by the following equation:

$$w(t) = \begin{cases} 0.5 - 0.5\cos\left(2\pi\dfrac{t-(T_D-T_{R1})}{2T_{R1}}\right) \\ \qquad (\text{if } T_D - T_{R1} \le t \le T_D + T_{R1}), \\ 0 \qquad (\text{otherwise}), \end{cases} \tag{27}$$

where the arrival time of the direct wave from the primary source at the observation point, T_D, is given by

$$T_D = \underset{t}{\text{argmax}}(s_{arr(x_O,y_O)}(t)) \tag{28}$$

where $\text{argmax}_t(\cdot)$ denotes the function that indicates the specific variable t to maximize the subject. Figure 24 shows the geometry of the primary source, the secondary source and the imaginary secondary source obtained by the image method. In Fig. 24, z_S denotes the distance from the floor surface to the secondary source. From this figure, T_{R1} is obtained as follows:

$$T_{R1} = \frac{r_{IO} - r_{SO}}{c}, \tag{29}$$

where r_{SO} and r_{IO} are written as

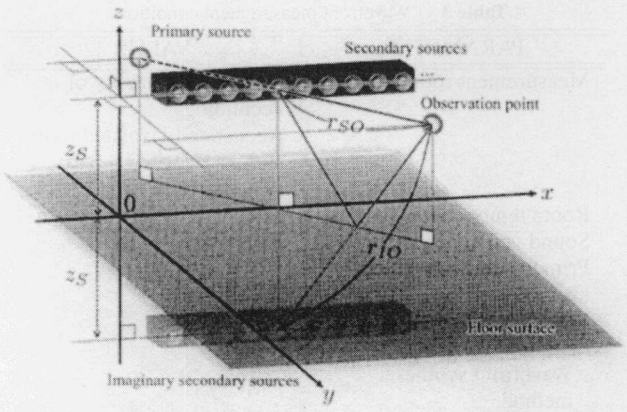

Fig. 24 Geometry of the primary source, the secondary sources and the imaginary secondary sources with the image method.

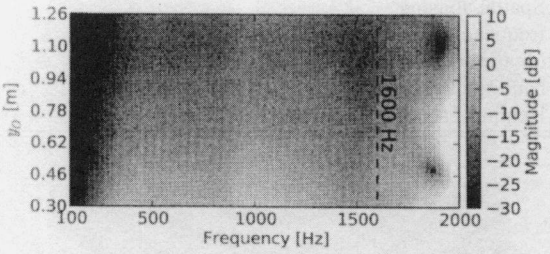

Fig. 25 Frequency-amplitude characteristics of the secondary wavefront in front of the primary sound source after the removal of the wavefront reflected from the wall surface.

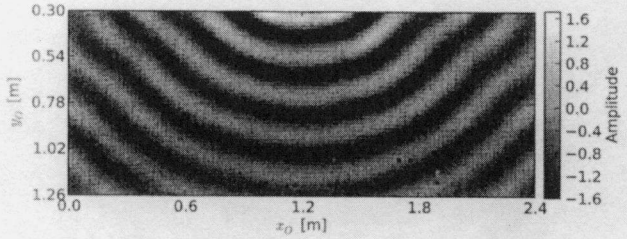

Fig. 26 Secondary wavefront after removal of reflected wavefront (1600 Hz).

$$r_{SO} = \sqrt{\left(x_O - \frac{y_O x_P - x_O y_P}{y_O - y_P}\right)^2 + {y_O}^2}, \tag{30}$$

$$r_{IO} = \sqrt{{r_{SO}}^2 + 4{z_S}^2}. \tag{31}$$

Figure 25 shows the frequency characteristics of the secondary wavefront in front of the primary source after the removal of the wavefront reflected from all of the wall surface in room. In this figure, the interference pattern shown in Fig. 20 is mitigated by the proposed window function for removal of the wavefront reflected from the wall surface. Therefore, it is predictable that the interference pattern is due to the wavefront reflected from the wall surface.

Figure 26 shows the secondary wavefront after the removal of the wavefront reflected in front of the primary sound source. By comparing this figure with Fig. 18, we can conclude that the reflected wavefront caused the interference

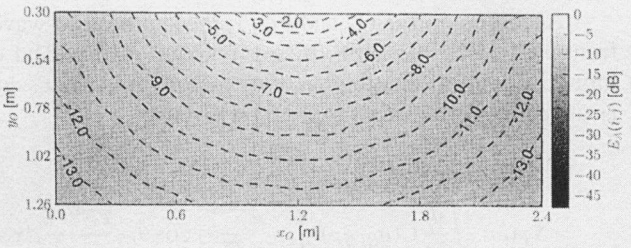

(a) E_A of the measured secondary wavefront (200–1400 Hz).

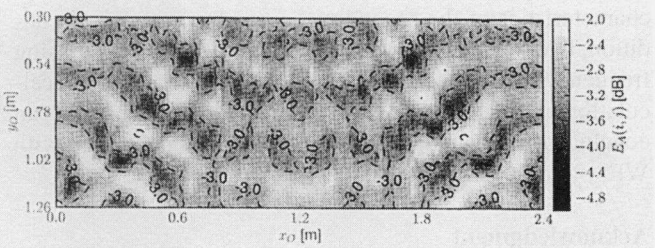

(b) E_P of the measured secondary wavefront (200–1400 Hz).

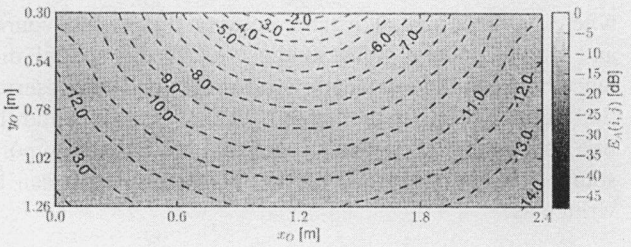

(c) E_A of the measured secondary wavefront (200–1600 Hz).

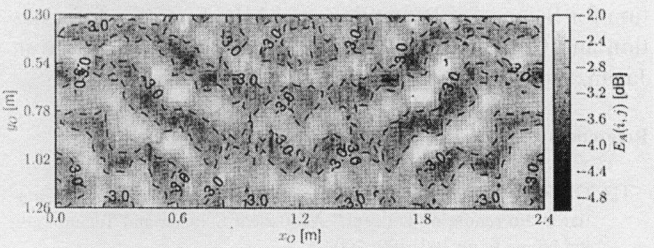

(d) E_P of the measured secondary wavefront (200–1600 Hz).

Fig. 27 Results of E_A and E_P with measured wavefront. Evaluated frequency bands are (a), (b) 200–1400 Hz and (c), (d) 200–1600 Hz.

observed in the measurement results because the wavefront interference is less evident in Fig. 26 is mitigated. In addition, DMCWS is performed above the WFS aliasing frequency (1417 Hz) in Fig. 26. Then, we evaluate the amplitude and phase error of measured wavefront using E_A and E_P in evaluated frequency band. Figure 27 shows the results of E_A and E_P with measured wavefront after removal of reflected wavefront. The lower limit of the evaluated frequency 200 Hz is determined by hardware (loudspeaker) limitation. The values of E_A and E_P are given on the contour lines, and the intervals between the contour lines are 1.0 dB in Figs. 27(a), 27(c). According to Figs. 27(a) and 27(c), the results of the amplitude and phase error E_A and E_P differ from that of the numerical simulations. In this paper, the filter calculation of DMCWS is premised on an anechoic reproduction environment. Therefore, the secondary wavefront accuracy decreases in practice owing to the inherent disadvantages of physical inaccuracies found in the DMCWS model characteristics described in Sect. 2.2.

5.6 Effect of Loudspeaker Frequency Characteristics on Measured Wavefront

To find the cause of the errors which are shown in the Fig. 27, we compare the frequency characteristics of the calculated, the measured after the removal of the reflected wavefront and that of the loudspeaker (Soundevice SD–0.6) at the observation point of $(x_O, y_O) = (1.2, 0.3)$ m in Fig. 28. According to the results, the measured characteristics are similar to those of the secondary source loudspeaker in the low-frequency subband with frequencies of up to 1600 Hz. Thus, the amplitude and phase error of the measured wavefront which shown in Fig. 27 can be attributed to the frequency-amplitude characteristics of the loudspeaker.

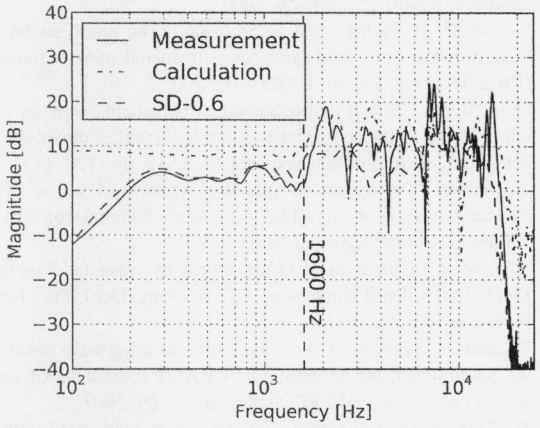

Fig. 28 Comparison of frequency characteristics of the loudspeaker and measured wavefront.

6. Conclusions

In this paper it has been shown that the accuracy of the synthesized secondary wavefront is related to the control-point coordinates and the wavefront measurement results of DMCWS in an actual environment. Numerical wavefront calculations clarified that the optimum y-coordinate of the directly aligned control point is $y_C = 0.6$–0.7 m. Also numerically obtained WFS and DMCWS wavefronts compared using this range of y_C that DMCWS has a larger listening area with fewer amplitude and phase errors than WFS, whereas they have a similar attenuation error.

Our wavefront measurement system and our algorithm using impulse responses measured in an acoustically isolated room clarified that the measured wavefront is affected by the mural-reflected wave and the frequency-amplitude

characteristics of the secondary source loudspeaker. In addition, DMCWS can be performed above the spatial aliasing frequency of WFS according to the results of numerical calculations and measurement. From these findings, we can conclude the advantageousness of DMCWS compared with WFS.

Acknowledgment

This work was partly supported by N·S Promotion Foundation for Science of Perception, and MIC Strategic Information and Communications R&D Promotion Programme in Japan.

References

[1] G. Theile and H. Wittek, "Wave field synthesis: A promising snatial audio rendering concent," Acoustical Science and Technology, vol.25, no.6, pp.393–399, 2004.
[2] N. Takashima, T. Sugano, S. Uto, and H. Harada, "The basic study of the sound field control using multi-channel adaptive digital filters," IEICE Technical Report, EA94-38, 1994.
[3] T. Ohno, H. Hokari, S. Shimada, and I. Oohira, "A study on cylindrical wave field synthesis with ultrasmall loudspeaker array," IEICE Technical Report, EA2006-56, 2006.
[4] S. Tanoue, H. Hokari, and S. Shimada, "The mono sound localization on the wave field synthesis with spatial transfer functions," IEICE Technical Report, EA2007-93, 2007.
[5] D. de Veries, "Sound reinforcement by wavefield synthesis: Adaptation of the synthesis operator to the loudspeaker directivity characteristics," J. Audio Eng. Soc., vol.44, no.12, pp.1120–1131, 1996.
[6] H. Wittek, "Perception of spatially synthesized sound fields—Literature review about WFS," http://www.hauptmikrofon.de/HW/Wittek_WFS_LitReview.pdf, 2003.
[7] E.W. Start, "Direct sound enhancement by wave field synthesis," Ph.D. Thesis, Delft University of Technology, Delft, Pays bas, The Netherlands, p.29, 1997.
[8] E. Corteel, "Synthesis of directional sources using wave field synthesis, possibilities, and limitations," EURASIP Journal on Advances in Signal Processing, vol.2007, Article ID 90509, 2007.
[9] H. Timo, "Two-way acoustic window using wave field synthesis," M. Thesis, Helsinki University of Technology, 2007.
[10] D.D. Rife and J. Vanderkooy, "Transfer-function measurement with maximum-length sequences," J. Audio Eng. Soc., vol.37, no.6, pp.419–443, 1989.
[11] J.B. Allen and D.A. Berkley, "Image method for efficiently simulating small-room acoustics," J. Acoust. Soc. Am., vol.65 no.4, pp.943–950, 1979.
[12] E. Corteel, Caractérisation et Extensions de la Wave Field Synthesis en conditions réelles d'écoute, Ph.D. thesis, Université de Paris VI, Paris, France, 2004.
[13] N. Bleistein, Mathematical methods for wave phenomena, Academic Press, Orlando, 1984.

Appendix: Derivation of Attenuation Law of WFS [12]

In this section, we introduce to estimate the radiation profiles of the synthesized wavefront emitted by an infinite line with the driving function obtained by WFS. Estimation in the frequency domain which is given by the stationary phase approximation [13] gives the attenuation law of synthesized wavefront.

According to Eq. (1) and Fig. 1, the synthesized wavefront emitted by the WFS driving function of the ideal of infinite size linear distribution of monopole sources (x_S, y_S) arranged along the x axis ($y_S = 0$) is given as

$$SWF(x_O, y_O, \omega) = S_P(\omega)\sqrt{\frac{\mathrm{j}k}{2\pi}}C(y_R, y_P)\int_{-\infty}^{\infty}\frac{e^{-\mathrm{j}kr_{PS}}}{\sqrt{r_{PS}}}\cos\theta_{PS}\frac{e^{-\mathrm{j}kr_{SO}}}{r_{SO}}dx_S, \tag{A·1}$$

where r_{PS} is the spatial distance between the primary source and the secondary point source, r_{SO} is the spatial distance between the secondary point source and the observation point and θ_{PS} is the angle between the y-axis and the line connecting the primary souce and the secondary point source. According to Eq. (A·1), the integral term can be written as

$$I(\omega) = \int_{\infty}^{\infty}\frac{e^{-\mathrm{j}kr_{PS}}}{\sqrt{r_{PS}}}\cos\theta_{PS}\frac{e^{-\mathrm{j}kr_{SO}}}{r_{SO}}dx_S = \int_{-\infty}^{\infty}f(x_S)e^{-\mathrm{j}k\chi(x_S)}dx_S, \tag{A·2}$$

where the functions $f(x_S)$ and $\chi(x_S)$ are given as

$$f(x_S) = \frac{1}{r_{SO}\sqrt{r_{PS}}}\cos\theta_{PS}, \tag{A·3}$$

$$\chi(x_S) = r_{SO} + r_{PS}. \tag{A·4}$$

The functions $f(x_S)$ and $\chi(x_S)$ are called envelope and phase function, respectively. $\chi(x_S)$ gives the derivatives of 1st and 2nd order as

$$\chi'(x_S) = \frac{x_S - x_P}{r_{PS}} - \frac{x_O - x_S}{r_{SO}} = \sin\theta_{PS} - \sin\theta_{SO}, \tag{A·5}$$

$$\chi''(x_S) = \frac{1}{r_{PS}} - \frac{(x_S - x_P)^2}{r_{PS}^3} + \frac{1}{r_{SO}} - \frac{(x_O - x_S)^2}{r_{SO}^3} = \frac{1}{r_{PS}} - \frac{\sin^2\theta_{SO}}{r_{PS}} + \frac{1}{r_{SO}} - \frac{\sin^2\theta_{PS}}{r_{SO}} = \frac{\cos^2\theta_{SO}}{r_{PS}} + \frac{\cos^2\theta_{PS}}{r_{SO}}, \tag{A·6}$$

where θ_{SO} is the angle between the y-axis and the line connecting the secondary point source and the observation point. The stationary phase approximation gives the estimation of this type of integral. Consider a phase point $x_S = x_{S0}$ for the phase function $\chi(x_S)$. We assume that the phase point x_{S0} satisfy the condition,

$$\begin{cases} \chi'(x_{S0}) = 0 \\ \chi''(x_{S0}) \neq 0 \end{cases}, \tag{A·7}$$

and the phase function admit an extremum only at x_{S0}. It is a maximum if $\chi''(x_{S0}) < 0$, if a minimum $\chi''(x_{S0}) > 0$. On either side of $x = x_{S0}$, the phase function is strictly monotonic

and thus the term $e^{-jk\chi(x_S)}$ is oscillatory. The point $x = x_{S0}$ is then called the stationary phase point. In this case, the stationary phase point x_{S0} is unique and given by

$$\theta_{SO} = \theta_{PS} = \theta_0. \tag{A·8}$$

Then, $f'(x_S)$ and $f''(x_S)$ which is the derivatives of 1st and 2nd order of $f(x_S)$ are continuous on $]-\infty \sim \infty[$, $f(x)$ is monotone around x_{S0}, and $f(x_{S0}) \neq 0$, the Taylor expansion around x_{S0} of expression under the integral gives:

$$f(x_S)e^{-jk\chi(x_S)} \approx f(x_{S0})e^{-jk\left[\chi(x_{S0})+\frac{(x_S-x_{S0})^2}{2}\chi''(x_{S0})\right]}. \tag{A·9}$$

Therefore, we obtain the approximation of $I(\omega)$ as

$$\begin{aligned}\hat{I}(\omega) &= \int_{-\infty}^{\infty} f(x_{S0})e^{-jk\left[\chi(x_0)+\frac{(x_S-x_{S0})^2}{2}\chi''(x_0)\right]}dx_S \\ &= f(x_{S0})e^{-jk\chi(x_{S0})}\int_{-\infty}^{\infty} e^{-jk\frac{(x_S-x_{S0})^2}{2}\chi''(x_{S0})}dx_S.\end{aligned} \tag{A·10}$$

In making the change of variable

$$\kappa = (x_S, x_{S0})\sqrt{\frac{k\chi''(x_{S0})}{2}}, \tag{A·11}$$

and provided that $\chi(x_{S0})'' \neq 0$, Equation (A·10) can be written as

$$\begin{aligned}\hat{I}(\omega) &= f(x_{S0})\sqrt{\frac{2\pi}{k|\chi''(x_{S0})|}}e^{-jk\chi(x_{S0})} \\ &\int_{-\infty}^{\infty} e^{-j\mathrm{sign}(k\chi''(x_{S0}))\kappa^2}d\kappa,\end{aligned} \tag{A·12}$$

where sign denotes the signum function. Note that

$$\int_{-\infty}^{\infty} e^{\pm j\kappa^2}d\kappa = \sqrt{\pi}e^{\pm\frac{\pi}{4}}, \tag{A·13}$$

the solution of the integral is given as

$$\hat{I}(\omega) = f(x_{S0})\sqrt{\frac{2\pi}{k|\chi''(x_{S0})|}}e^{-j\left[k\chi(x_{S0})+\mathrm{sign}(\chi''(x_{S0}))\frac{\pi}{4}\right]} \tag{A·14}$$

From Eqs. (A·6) and (A·8), $\chi''(x_{S0})$ is given as

$$\chi''(x_{S0}) = \cos^2\theta_0\left(\frac{1}{r_{PS0}} + \frac{1}{r_{SO0}}\right), \tag{A·15}$$

where r_{PS0} and r_{SO0} are r_{PS} and r_{SO} in the stationary phase point, respectively. Finally, the pressure of the synthesized wavefront $SWF(x_O, y_O, \omega)$ can be rewritten as

$$\begin{aligned}&SWF(x_O, y_O, \omega) \\ &= S_P(\omega)\sqrt{\frac{jk}{2\pi}}C(y_R, y_P)\hat{I}(\omega) \\ &= S_P(\omega)C(y_R, y_P)\sqrt{\frac{r_{PS0}-r_{SO0}}{r_{SO0}}}\frac{e^{-jk(r_{PS0}+r_{SO0})}}{r_{PS0}+r_{SO0}}.\end{aligned} \tag{A·16}$$

From this equation, the pressure law in front of the primary source can be written as

$$SWF(y_O, \omega) = S_P(\omega)\sqrt{\frac{|y_R|}{|y_O|}}\sqrt{\frac{|y_O|+|y_P|}{|y_R|+|y_P|}}\frac{e^{-jk|y_O-y_P|}}{|y_O-y_P|}. \tag{A·17}$$

Therefore, we obtain the attenuation law denoted in Eq. (3).

Noriyoshi Kamado was born in Okayama, Japan, in 1984. He received the B.E. degree in Electrical and Mechanical System Engineering Advanced Courses, Nagaoka National College of Technology in 2007, and the M.E. degree in Electrical and Electronic Systems Engineering from Nagaoka University of Technology in 2009. He is currently a Ph.D. student at the Graduate school of Information Science, Nara Institute of Science and Technology. His research interests include digital signal processing for sound field coding, reproduction and psychoacoustics. He is a member of the Acoustical Society of Japan and Audio Engineering Society (AES).

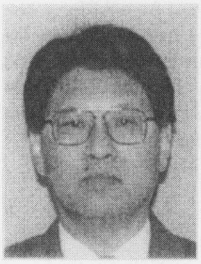

Haruhide Hokari was born in Niigata, Japan, in 1949. He graduated from the mechanical engineering department of Nagaoka Technical Senior School, Niigata, Japan, in 1969, and was a technical official of the Niigata University until 1979. He joined the Nagaoka University of Technology in 1979, where he is a technical official in the Electrical Department. His reserch and development work includes telepresence communication system and psychoacoustics. He is a member of the Acoustical Society of Japan.

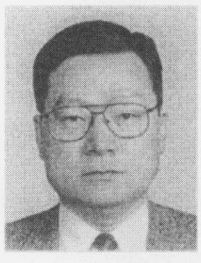

Shoji Shimada was born in Yokohama, Japan, in 1945. He received the B.E. degree in 1968 and the M.S. degree in 1970 from Waseda University. He joined the Electrical Communication Laboratories of NTT in 1970, where he worked on digital signal processing technologies for the network system. From 1977 to 1988 he was a member of ITU-T (CCITT) SG XV & SG XVII. While a member of SG XV, he worked as the special rapporteur on the acoustic echo canceller. He received the Ph.D. degree from Waseda University in 1988, and joined the Nagaoka University of Technology in 1993, where he is a professor of information transmission systems in the Electrical Department. His research and development work includes digital signal processing technologies of sound telecommunications and psychoacoustical sound localization. He is a member of the Audio Engineering Society, IEEE, EURSIP, the Acoustical Society of Japan.

Hiroshi Saruwatari was born in Nagoya, Japan, on July 27, 1967. He received the B.E., M.E. and Ph.D. degrees in electrical engineering from Nagoya University, Nagoya, Japan, in 1991, 1993 and 2000, respectively. He joined Intelligent Systems Laboratory, SECOM CO., LTD., Mitaka, Tokyo, Japan, in 1993, where he engaged in the research and development on the ultrasonic array system for the acoustic imaging. He is currently an associate professor of Graduate School of Information Science, Nara Institute of Science and Technology. His research interests include array signal processing, blind source separation, and sound field reproduction. He received the Paper Awards from IEICE in 2001 and 2006, and from TAF in 2003. He is a member of the IEEE and the Acoustical Society of Japan.

Kiyohiro Shikano received the B.S., M.S., and Ph.D. degrees in electrical engineering from Nagoya University in 1970, 1972, and 1980, respectively. He is currently a professor of Nara Institute of Science and Technology (NAIST), where he is directing speech and acoustics laboratory. From 1972 to 1993, he had been working at NTT Laboratories. During 1986–1990, he was the Head of Speech Processing Department at ATR Interpreting Telephony Research Laboratories. During 1984–1986, he was a visiting scientist in Carnegie Mellon University. He received the Yonezawa Prize from IEICE in 1975, the Signal Processing Society 1990 Senior Award from IEEE in 1991, the Technical Development Award from ASJ in 1994, IPSJ Yamashita SIG Research Award in 2000, and Paper Award from the Virtual Reality Society of Japan in 2001, IEICE paper award in 2005 and 2006, and Inose award in 2005. He is a fellow of the Institute of Electrical and Electronics, Engineers (IEEE) and Information Processing Society of Japan, and a member of the Acoustical Society of Japan (ASJ), Japan VR Society, and International Speech Communication Society (ISCA).